nature astronomy

Article

https://doi.org/10.1038/s41550-024-02428-z

Combined analysis of the 12.8 and 15 µm JWST/MIRI eclipse observations of TRAPPIST-1 b

Received: 4 December 2023

Accepted: 29 October 2024

Published online: 16 December 2024

Check for updates

A list of authors and their affiliations appears at the end of the paper

The first James Webb Space Telescope/MIRI photometric observations of TRAPPIST-1 b allowed for the detection of the thermal emission of the planet at 15 µm, suggesting that the planet could be a bare rock with a zero albedo and no redistribution of heat. These observations at 15 µm were acquired as part of Guaranteed Time Observer time that included a twin programme at 12.8 µm to obtain measurements inside and outside the CO_2 absorption band. Here we present five new occultations of TRAPPIST-1 b observed with MIRI in an additional photometric band at 12.8 µm. We perform a global fit of the ten eclipses and derive a planet-to-star flux ratio and 1σ error of 452 ± 86 ppm and 775 ± 90 ppm at 12.8 µm and 15 µm, respectively. We find that two main scenarios emerge. An airless planet model with an unweathered (fresh) ultramafic surface, that could be indicative of relatively recent geological processes, fits the data well. Alternatively, a thick, pure-CO_2 atmosphere with photochemical hazes that create a temperature inversion and result in the CO_2 feature being seen in emission also works, although with some caveats. Our results highlight the challenges in accurately determining a planet's atmospheric or surface nature solely from broadband filter measurements of its emission, but also point towards two very interesting scenarios that will be further investigated with the forthcoming phase curve of TRAPPIST-1 b.

At the time of writing, no atmosphere has been detected around any known temperate ($0.1S_{Earth} < S_p < 5S_{Earth}$) rocky planet outside our solar system. However, with the James Webb Space Telescope (JWST) it is now possible to search for atmospheres around such planets, notably around the latest red dwarfs (spectral types later than M6, and effective temperature less than 3,000 K; ref. 1), also called ultracool dwarf stars. The small sizes of such ultracool dwarfs yield favourable planet-to-star radius ratios, enabling atmospheric studies of terrestrial planets. Among the ~5,500 exoplanets that have been confirmed so far, only 17 of them can be classified as probably rocky and orbiting ultracool dwarf stars[2–8]. In particular, 7 of these 17 planets belong to the same system, the TRAPPIST-1 system. Due to their transiting nature, combined with the infrared brightness and the small size of their host star, as well as the resonant architecture of the system that allows mass measurements via the transit timing variation (TTV) method, the TRAPPIST-1 planets are currently the best known terrestrial planets beyond our own Solar System[9]. For all these reasons, TRAPPIST-1 has been identified as a prime target for JWST[10,11], as emphasized by the ten programmes dedicated to the characterization of the system in the first 3 years of JWST's operation. These programmes are the following: Guaranteed Time Observer (GTO) 1177 (principal investigator, PI: T.G.), GTO 1279 (PI: P.-O.L.), GTO 1201 (PI: Lafranière), GTO 1331 (PI: Lewis), Guest Observer (GO) 2589 (PI: Lim), GO 2304 (PI: Kreidberg), GO 2420 (PI: Rathcke), GO 1981 (PIs: Lustig-Yaeger and Stevenson), GO 3077 (PIs: M. Gillon and E.D.), GO 5191 (PIs: E.D. and P.-O.L.). This represents a total of ~290 h of observation. Among these ten programmes, three were dedicated to

e-mail: elsa.ducrot@cea.fr

the observation of the secondary eclipses (when the exoplanet moves out of sight behind the star) of the two innermost planets, TRAPPIST-1 b and c. As part of GTO 1177 and GO 2304, five eclipses of TRAPPIST-1 b and four eclipses of TRAPPIST-1 c were observed using the MIRI imaging F1500W filter. For planet b, the brightness temperature at 15 μm derived from the secondary eclipses suggested that the planet has little to no planetary atmosphere redistributing radiation from the host star[12]. For planet c, the eclipse depth at 15 μm suggested that, if the planet had an atmosphere, it was probably thin and not enriched in CO_2 (ref. 13).

Examining the thermal emission of a planet in the mid-infrared (IR) as it experiences its secondary eclipse is a powerful way to constrain the presence of an atmosphere[14–16]. The depth of the eclipse can be used to measure the dayside flux of the planet in a specific bandpass. Furthermore, unlike transit spectroscopy, thermal emission remains immune to spectral contamination from the host star (via the transit light source effect[17]), and the impact of flares and rotational modulation is minimal in the mid-IR and should thus be much less of a concern than for transmission spectroscopy at shorter wavelengths. Cycle 1 observations of TRAPPIST-1 have shown that flare events occur during most transit observations and have intensities up to several thousand ppm in the near infrared, of similar order to the transit depth signals[18,19]. These incessant eruptions combined with the transit light source effect complicate the interpretation of transmission spectra to the point where substantially more transits than predicted will be needed to detect putative secondary atmospheres on the TRAPPIST-1 planets. For these reasons, and until a systematic method to properly correct for the transit light source effect is developed, emission (spectro)-photometry is the best avenue to put constraints on the nature of the TRAPPIST-1 planets.

We present the results from the third TRAPPIST-1 emission programme thus far, which was taken as part of the ExO-MIRI consortium (GTO 1279). This consists of the observation of five eclipses of TRAPPIST-1 b with MIRI using the F1280W filter (spanning wavelengths from 11.588 μm to 14.155 μm), to be compared with those obtained with the F1500W filter (spanning wavelengths from 13.527 μm to 16.640 μm) and presented in ref. 12.

The F1280W filter strikes an appropriate balance between photometric precision and planet-to-star flux contrast, allowing for the detection of the thermal emission of a planet whose expected dayside temperature is ~500 K, in orbit around an ultracool star whose effective temperature is 2,566 ± 26 K (ref. 9). The observations took place on 21 November 2022 and on 6, 7, 15 and 23 July 2023. Due to a change in the observing strategy between the first visit and the four others, the observations had a duration of 3.21–3.88 h, and the eclipses lasted 36 min each; see Extended Data Table 1 for details. The required dates and times of the observations were estimated from the TTV analysis in ref. 9 and selected so that there was no contamination by simultaneous transits, secondary eclipses or planet–planet occultations[20] of other planets in the system.

Results

We performed four independent data reductions using Eureka![21] and a custom pipeline (Extended Data Table 2). For each pipeline, light curves were derived using aperture photometry as discussed in Methods. The light curves obtained for each visit from the four distinct reduction pipelines led to consistent photometric precision (Extended Data Table 2). Three distinct Bayesian data analyses of the light curves were then carried out with various methods for the sampling of the posterior probability distributions of the system's parameters and one more empirical approach was carried out (Methods). Each Bayesian analysis included individual fits of each visit, a global fit of the five eclipses and, for two of them (ED and MG), a generalized global fit including all ten MIRI JWST eclipses of TRAPPIST-1 b (five at 15 μm and five at 12.8 μm). For each Bayesian analysis, we fitted for an eclipse model with a specific parametrization, as well as for systematic effects, which can include a time-dependent polynomial, exponential ramps and decorrelation against the position and full-width at half-maximum (FWHM) of the point spread function (PSF).

The four distinct reductions led to consistent light curves for which the root mean square of the residuals among all data reductions ranges between 672 ppm and 963 ppm (10–20% more precise than reported at 15 μm in ref. 13).

The eclipse depth of each visit is estimated using distinct approaches with various sampling methods (Markov chain Monte Carlo (MCMC) or nested sampling) with different sets of parameters for the astrophysical model and the instrumental systematic model (Extended Data Table 3).

The derived values from individual fits, joint fits and generalized fits are presented in Extended Data Table 4. To determine the definitive value of the eclipse depth at 12.8 and 15 μm, we performed an additional joint analysis that we call the 'fiducial analysis', for which we used the light curves derived from the reduction with the best photometric precision (MG, Extended Data Table 2) and then apply a different baseline for the systematic model to simplify it, detrending only in time, position and FWHM with a restriction to not use polynomials with degree of >2 to prevent overfitting. The detrended phase-folded light curves at 12.8 μm and at 15 μm from the fiducial global fit of all ten eclipses are shown in Fig. 1. We note that all our analyses are consistent with each other (Methods). The final eclipse depths, and their 1σ uncertainties, are $(F_p/F_\star)_{b,\,12.8\,\mu m} = 452 \pm 86$ ppm and $(F_p/F_\star)_{b,\,15\,\mu m} = 775 \pm 90$ ppm. The eclipse depth computed at 15 μm is in agreement at the 1σ level with the one already published ($(F_p/F_\star)_{b,\,15\,\mu m,\,Greene+2023} = 863 \pm 99$ ppm; ref. 12), as shown in Extended Data Fig. 1.

From these eclipse depth values, we derive corresponding blackbody brightness temperatures and 1σ uncertainties of $T_{bright,\,12.8\,\mu m} = 424 \pm 28$ K and $T_{bright,\,15\,\mu m} = 478 \pm 27$ K at 12.8 μm and 15 μm, respectively (see Methods for details of these calculations). Our new estimation of the brightness temperature at 15 μm, from the joint fit of all ten eclipses, is thus in agreement at the 1σ level with the one derived in ref. 12 ($T_{bright,\,15\,\mu m,\,Greene+2023} = 503 \pm 27$ K). However, the brightness temperature that we derive at 12.8 μm is in disagreement at the 2.1σ level with that expected from the almost null-albedo bare-rock scenario as initially favoured by ref. 12 (503 ± 26 K). This result suggests that the nature of TRAPPIST-1 b is potentially more complex than initially expected from the 15 μm observations alone.

Discussion

Now that we have measurements of the flux emitted by TRAPPIST-1 b in two distinct bands, we can compare them with some surface and atmospheric models. First, we compute the Bond albedo (A_B) of the planet by fitting the theoretical emission of a bare rock with no redistribution of heat and albedo as free parameter. We model this theoretical emission spectrum by considering the planetary flux to be a sum of blackbodies calculated for a grid of $T(\theta, \phi)$, where θ and ϕ are the longitude and the latitude, respectively (see Methods for more details). The resulting emission spectra for $A_B = 0$, 0.2, 0.4 are shown as dashed lines in Fig. 2.

The resulting best-fit Bond albedo and its 1σ uncertainty are $A_B = 0.19 \pm 0.08$ (see details of how this value is computed in Methods). This value is relatively high for a supposedly bare rock that would have endured billions of years of space weathering. Atmosphereless planets are exposed to the impacts of micrometeorites and stellar irradiation, which tend to cover the surface with nanoparticles of metallic iron, resulting in a lowering of the planet's albedo (more details in ref. 22). As a comparison, the Bond albedo of Mercury is 0.08 (refs. 23,24). For close-in planets around active stars, such as TRAPPIST-1 b, the timescale of space weathering processes is expected to be much shorter, of the order of 10^2–10^3 yr (ref. 13). In addition, ref. 14 demonstrated that observations of a bare rock surface lead to inference of a Bond albedo lower than that of the real surface.

https://doi.org/10.1038/s41550-024-02428-z

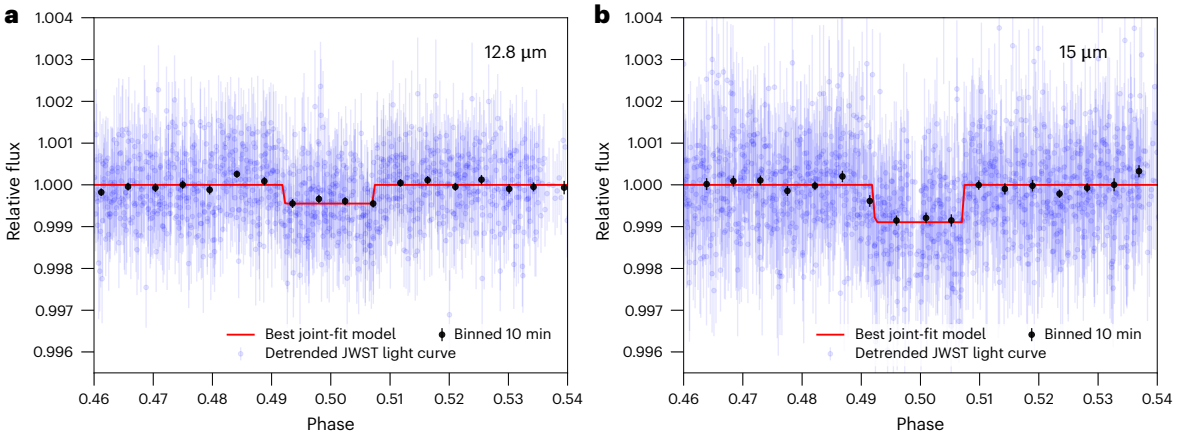

Fig. 1 | Phase-folded JWST/MIRI observations of TRAPPIST-1 b. a, Phase-folded light curve of the secondary eclipse of TRAPPIST-1 b at 12.8 µm, derived from the observations of five eclipses as part of GTO 1279. **b**, Phase-folded light curve of the secondary eclipse of TRAPPIST-1 b at 15 µm, derived from re-analyses of the observations of five eclipses as part of GTO 1177. These figures are derived from the fiducial analysis described in Methods. Blue dots correspond to the corrected flux at the original time of sampling, black dots show the 10-min-binned corrected flux with an error equal to the s.d. of the points within the bin, and the red curve shows the eclipse model.

First, we compare our data with the set of plausible surface models (given the level of irradiation received by TRAPPIST-1 b) presented by ref. 25, including basaltic, ultramafic, feldspathic, metal rich, Fe oxidized (a mixture of basalt and nanophase haematite) and granitoid[14,26]. We find that the measured planetary flux is most consistent with an ultramafic rock (Methods) composed of 60% olivine and 40% enstatite.

In all the models, the rocks were considered to be geologically fresh. For older surfaces ($\geq 10^3$ yr) we expect notable impacts of space weathering, resulting in increased eclipse depth in the F1280W and F1500W bands, consequently deteriorating the fit. The presence of fresh ultramafic rock on the surface of TRAPPIST-1 b would be very interesting, as it could indicate recent surface processing. Several geological processes such as volcanism resurfacing or crustal reprocessing due to tectonic recycling could explain a more recent surface. TRAPPIST-1 b is expected to experience strong tidal heating due to its close proximity to its star and the perpetual excitation of its eccentricity by the other planets[27]. The planet is also expected to endure induction heating, due to the large magnetic field of its host star[28]. The combination of these effects should result in a substantial increase of volcanic activity. TRAPPIST-1 b could, therefore, be compared with Io, which has a surface so young that it has no impact craters. In this context, the scenario of an airless TRAPPIST-1 b with a young ultramafic surface seems probable.

Second, we compare our data with plausible atmospheric models. The initial goal of GTO programme 1177 and GTO programme 1279 was to measure the planetary flux inside and outside the CO_2 absorption band (centred around 15 µm) to investigate the presence of an atmosphere and possibly CO_2 at the same time. An atmosphere where the opacity is dominated by greenhouse gases such as CO_2 is expected to have a temperature increasing with pressure. Thus, at 15 µm, where CO_2 is strongly absorbing, we would measure the temperature high up in the atmosphere, resulting in a lower brightness temperature at 15 µm than at 12.8 µm, where we can look deeper into the atmosphere. However, our observations suggest the opposite. Within this framework, we explore the possibility that this can be explained by a thermal inversion, where the upper atmosphere is hotter than the atmosphere below, creating a CO_2 emission feature instead of a CO_2 absorption feature. Such a thermal inversion is observed in the atmosphere of many planets in the Solar System and also in Titan's atmosphere. It is characteristic of a transition to the stratosphere, typically around a pressure level of 0.1 bar, and is mainly produced by heating through haze absorption[29]. The hazes, which are efficient absorbers of stellar radiation, create an inverse greenhouse effect by absorbing the stellar radiation high up in the atmosphere, heating the upper atmosphere and cooling the atmosphere below. Interestingly, the hazes in the atmosphere of Titan are expected to be formed from ultraviolet (UV) photochemistry. Similarly, hazes could form in the atmosphere of TRAPPIST-1 b through efficient photodissociation resulting from the much stronger extreme UV (EUV) of TRAPPIST-1 and the proximity of the planet to its star[30–32] (Extended Data Fig. 2 and Methods).We note that this thermal inversion is not observed in the atmosphere of Venus, which is temperature-wise

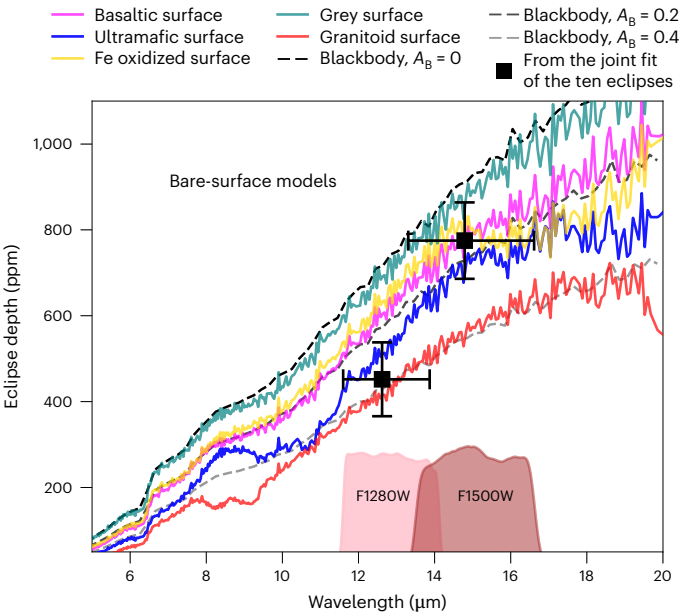

Fig. 2 | TRAPPIST-1 b's emission spectrum, compared with bare-surface models. Measurements of the eclipse depth of TRAPPIST-1 b in the 12.8 µm and 15 µm bands resulting from five visits in each band with their 1σ uncertainties from our fiducial joint analysis (MCMC analysis detailed in Methods), compared with realistic emission models for bare-surface models from ref. 25. The measurements are centred on the effective wavelength, which is computed by weighting the throughput of the filter with the corrected SPHINX synthetic stellar spectrum (see Methods for details). The error bar in wavelength stands for the width of the filter in each band. Coloured markers show the band-integrated depth value for each model. Red and brown filled areas show the responses of the F1280W and F1500W filters, respectively.

https://doi.org/10.1038/s41550-024-02428-z

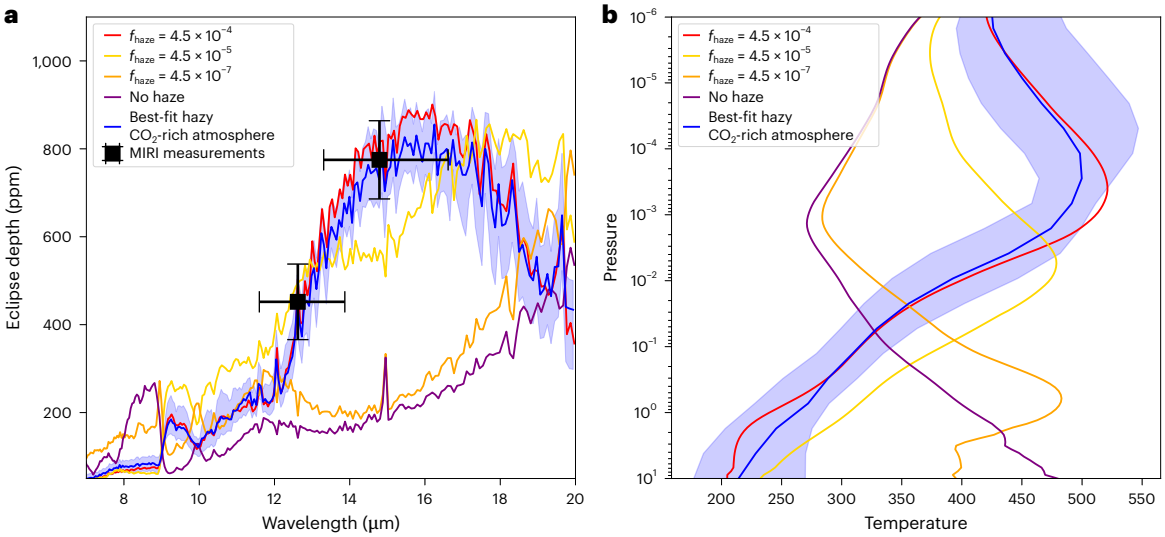

Fig. 3 | Best-fit atmosphere model is a hazy CO_2-rich atmosphere. a,**b**, Eclipse spectrum (**a**) and temperature structure (**b**) for the haze atmosphere models. Model calculations are shown for haze mass fractions (f_{haze}) of 4.5×10^{-4}, 4.5×10^{-5} and 4.5×10^{-7} as well as for our best-fit solution (blue line) and its 1σ uncertainty interval (blue shading). In **a**, the MIRI observations, resulting from five visits in each band, are shown by black squares and their 1σ errors derived from our fiducial joint analysis are shown by black error bars. The measurements are centred on the effective wavelength, which is computed by weighting the throughput of the filter with the corrected SPHINX synthetic stellar spectrum (see Methods for details). The error bar in wavelength stands for the width of the filter in each band.

the most similar to TRAPPIST-1 b in our Solar System. This is probably because of the dominance of highly scattering condensation clouds in the atmosphere of Venus.

Using a hazy atmospheric set-up inspired by the Titan atmosphere, we show that for a thick, CO_2-rich atmosphere with photochemical haze our model can fit the measurements very well (Fig. 2). Indeed, the presence of hazes results in a strong thermal inversion, causing CO_2 to appear in emission (Fig. 3). The mixing ratio of hazes seems modest at first glance, but more detailed modelling would be required to assess the feasibility of this level of hazes in the atmosphere. This scenario is interesting as it highlights the importance of thermal inversions in the interpretation of planetary emission spectra. However, it comes with some caveats concerning the haze formation and climate stability. For instance, on Titan hydrocarbon hazes are formed through CH_4 photodissociation, but in the case of a hot, CO_2-rich TRAPPIST-1 b the co-existence of CH_4 and CO_2 is photochemically[33] and thermodynamically[34] implausible. However, ref. 35 showed that the formation of hydrocarbon hazes is experimentally possible without CH_4 in a hot, CO_2-rich atmosphere that possesses H_2S, although it is unclear yet whether the requisite 1% H_2S abundances can be maintained by volcanism in comparatively oxidized, CO_2-dominated terrestrial atmospheres. In that context, this proposed atmospheric scenario is less likely that the bare-surface one, but still worth investigating experimentally and theoretically.

Our work shows how the measured thermal flux of TRAPPIST-1 b in the F1280W and F1500W MIRI filters can be fitted with either an airless surface model (potentially with a fresh ultramafic composition) or a thick, CO_2-rich atmosphere containing photochemical hazes. Even if the airless scenario is physically more plausible, the existence of an atmosphere around TRAPPIST-1 b still remains undetermined. Importantly, we predict that the simultaneous phase curve measurement at 15 μm of TRAPPIST-1 b and c obtained as part of GO programme 3077 will allow us to distinguish between a dense, CO_2-rich atmosphere and an airless ultramafic rock (Methods).

These results motivate additional observations of TRAPPIST-1 b in emission in distinct bands with JWST, as well as further considerations of thermal inversion in planetary atmospheres in the presence of photochemical hazes. Furthermore, our work highlights how the degeneracy of emission models can complicate the interpretation of broadband measurements. It is currently not possible to reach a definitive conclusion with only two measurements of the planetary thermal flux, a finding that has major implications for other programmes seeking to study rocky worlds with emission photometry (for example, the Hot Rocks Survey, GO programme 3730, and the Survey of Rocky Worlds, recently recommended for a Director's Discretionary Time Concept[36]). However, we predict that the combination of broadband emission spectra with photometric phase curve observations offers a robust method to assess the presence of atmospheres around rocky planets.

Methods

Observations

Observations were performed as part of GTO 1279 (PI: P.-O.L.) in November 2022 and July 2023 (Extended Data Table 1). The observation strategy used for the first eclipse (in November 2022) was slightly different from that used for the four others. Initially the strategy was to offset TRAPPIST-1 from the centre of the detector to allow for a second star in the field. The justification for this offset was to use this second star for systematic correction. However, as the amplitude of the detector effects observed with MIRI imaging turned out to be dependent on the flux of the star, this second star was not as useful as expected. Additionally, TRAPPIST-1 was offset to the edge of the detector, where the quality of the flat taken at 12.8 μm was slightly worse. As this strategy was adding more constraints to the observations for no substantial gain, we decided against utilizing it for the four other eclipses, instead opting to place TRAPPIST-1 at the centre of the detector. Supplementary Fig. 1 shows the detector's first images for the first and second visits with TRAPPIST-1 indicated in red.

Data reduction

Four distinct reductions of the data were performed to ensure consistency of the results. A summary of the different settings for each reduction is given in Extended Data Table 2, with detailed explanations given in the sections below.

Data reduction ED. For the first data reduction, we employed the Eureka! pipeline[21] from stages 1 to 4. Our process began with the uncal.fits files, utilizing the default JWST pipeline settings. In stage 1, we tried

setting the ramp-fitting weighting parameters to default and then uniform to see if this improved the root mean square of our residuals. The difference being marginal, we decided to keep the default ramp-fitting weighting set-up, assigning more weight to the first and last groups. In stage 2, we deactivated the photom step. Moving on to stage 3, we defined a subarray region ([642, 742], [460, 560] for the first visit and [642, 742], [460, 560] for the four others), masked pixels flagged in the DQ array, interpolated defective pixels and conducted aperture photometry on the star. We chose an aperture of 5 pixels for each visit. For each integration, we recorded the centre and width of the PSF in the x and y directions by fitting a two-dimensional Gaussian. Background computation involved an annulus with radii of 12–30 pixels (centred on the target), with the result subtracted. We underline that the choice of the background annulus minimally influenced the light curve. In stage 4, we applied a 4σ sigma-clip to identify outliers deviating from the median flux, calculated using a 20-integration-width boxcar filter.

Data reduction MG. The second data reduction used the following methodology. The raw uncal.fits files were first calibrated using the first stage of the Eureka! pipeline[21] and the second stage of the JWST pipeline. A systematic exploration of all the combinations of all Eureka! stage 1 options identified the combination resulting in the most precise light curves. It corresponded to the default JWST pipeline settings, except for setting the ramp-fitting weighting parameter to uniform, and the deactivation of the jump correction. The rest of the reduction was done using a pipeline coded in IRAF and Fortran 2003, which performed the following steps for each image: (1) a change of unit from MJy sr^{-1} to recorded electrons, (2) the fit of a two-dimensional Gaussian function on the profile of TRAPPIST-1 to measure the subpixel position of its centroid and its FWHM in both directions and (3) the measurement of the stellar and background fluxes using circular and annular apertures, respectively, with IRAF/DAOPHOT[37]. Finally, the resulting light curves were normalized and outliers were discarded using a 4σ clipping with a 20 min moving median algorithm (average fraction of clipped points: 3.5%). For each visit, the radius of the circular aperture used to measure the stellar flux was optimized by minimizing the s.d. of the residuals. Apertures of 3.5 pixels were used for all programme 1177 data. For programme 1279 data, an aperture of 3.5 pixels was used for the first light curve, and 3.8 pixels for the four others. The background was measured in an annulus going from 30 to 45 pixels from the PSF centre. For each stellar flux measurement, the corresponding error was computed taking into account the star and background photon noise, the readout noise and the dark noise, and assuming a value of 3.1 electrons per analogue-to-digital unit for the gain.

Data reduction TJB. The third data reduction method started from the _uncal.fits files and followed the general procedure of ref. 12 with a few differences. This reduction used v.0.9 of the Eureka! data analysis pipeline[21], with JWST calibration pipeline v.1.10.2 (ref. 38), Calibration Reference Data System (CRDS) v.11.17.0 (ref. 39) and the jwst_1106.pmap CRDS context. Stage 1 was run with the firstframe and lastframe steps turned on and the jump rejection threshold set to 10σ. Stage 2 was run with the photom step turned off. Stage 3 assumed a gain of 3.5 electrons per data number, performed a double-iteration 5σ clipping along the entire time axis for each pixel, used a circular annulus with radii of 14 and 34 pixels to remove the background flux, extracted the source flux using a circular aperture with a radius of 8 pixels and computed the source (x, y) location and PSF width as a function of time to later use as covariates when fitting the light curve. Finally, in stage 4 we clipped 3σ outliers, compared with a 10-integration-wide boxcar-filtered version of the data.

Data reduction POL. The fourth data reduction and analysis was carried out in a different manner when compared with the three previous ones. The starting point is the uncalibrated data. We have $N_{\rm frames} \times N_{\rm integrations}$ images with 1,032 × 1,024 pixels, where $N_{\rm frames}$ is the number of frames per integration and $N_{\rm integrations}$ is the number of integrations during the exposure. The data are in the form of an array with four dimensions: 1,032, 1,024, $N_{\rm frames}$, $N_{\rm integrations}$; the values of these parameters according to the observations are given in Extended Data Table 1. The data reduction is achieved with a homemade pipeline using the IDL language. The first step is to reduce the size of the images from a 1,032 × 1,024 pixel array to a 101 × 101 pixel array, centred on the maximum of signal of the PSF of the TRAPPIST-1 star. Then we apply the nonlinearity correction to each pixel of the $N_{\rm frames} \times N_{\rm integrations}$ images; for this we use the jwst_miri_linearity_0039.fits file from the JWST CRDS. Because of the so-called last-frame effect, we disregard the last frame and consider the signal (in digital number) at the frame number $N_{\rm frames} - 1$); we are working with an array with three dimensions: (101, 101, $N_{\rm integrations}$). The jitter amplitude is computed with the IDLGCNTRD routine using a box with a half-width of 4 pixels centred on the pixel with the maximum signal. As expected, the jitter amplitude is very low (less than 1 mas). There are a number of centroid positions that deviate from the mean position by more than 3σ; the root cause is not telescope jitter (we do not see any effect in our data even when there is a high-gain antenna move) but probably cosmic-ray impacts. Indeed, when a cosmic ray hits the zone of interest, it changes the signal in the various pixels of the box in an inhomogeneous way, changing the position of the centroid. Then we apply an aper-imaIDL function, which calculates the sum of the signal in the 57 pixels inside a radius of 4 pixels centred on the pixel with the maximum of signal. This is possible because of the great stability of the telescope. At this point, we have an array with one dimension containing the aperture signal as a function of the integration number. To remove outliers, we take advantage of having $N_{\rm frames}$ per integration. We calculate the difference of signal between two consecutive frames, then the mean of the values over time and the noise using the meanclipIDL function. We reject the integrations for which one frame difference is 5σ off the mean. We discard 8% of the frames.

Data analysis

We used four distinct data analysis approaches. For each approach, we performed independent fits of each individual eclipse as well as performing a joint fit of all eclipses at each wavelength. Then, for two of the approaches we performed an additional global joint fit of all ten eclipses together. The results from these analyses are summarized in Extended Data Table 4.

Data analysis ED. After acquiring the light curve for each visit in stage 4 of the Eureka! pipeline, we employed the Fortran code trafit, a modified version of the adaptive MCMC code discussed in refs. 40,41. This code utilizes the eclipse model from ref. 42 as a photometric time series, multiplied by a baseline model that represents various astrophysical and instrumental systematics contributing to photometric variations. Initially, we individually fitted all visits, exploring a broad range of baseline models to accommodate different sources of flux variation/modulation, such as instrumental and stellar effects. This encompassed polynomials of varying orders concerning time, background, PSF position on the detector (x, y) and PSF width (in x and y). Upon selecting the baseline, we conducted a preliminary analysis with a single Markov chain comprising 50,000 steps to assess the need for rescaling photometric errors. This involved considering potential underestimation or overestimation of the white noise in each measurement and the presence of time-correlated (red) noise in the light curve. After adjusting the photometric errors, two Markov chains of 100,000 steps each were run to sample the probability density functions of the model parameters and the physical system parameters. The convergence of the MCMC analysis was evaluated using the Gelman and Rubin statistical test. For each individual analysis, jump parameters with normal distributions were employed: $M_\star$, $R_\star$, $T_{\rm eff}$, [Fe/H], t_0, b and eccentricity e, where $T_{\rm eff}$

is the effective temperature of the star, t_0 is the transit mid time and b is the impact parameter of the planet All priors were adopted from refs. 9,43. The values of orbital period P and orbital inclination i were fixed to the literature values provided in the cited references. The resulting eclipse depths are given in Extended Data Table 4.

We then performed a global analysis with all five visits at 12.8 µm and all five visits at 15 µm. The baseline models, derived from our individual fits for each light curve, were employed. Once again, a preliminary run involving a single chain of 50,000 steps was executed to estimate uncertainty correction factors, which were then applied to the photometric error bars. This was followed by a second run with two chains of 100,000 steps. The jump parameters mirrored those used in the individual fits, with the exception that t_0 was fixed, and allowance was made for TTVs to occur for each visit. For each TTV, an unconstrained uniform prior was centred on the predicted value from ref. 9. The Gelman and Rubin statistic was utilized to evaluate the convergence of the fit.

Finally, a global analysis was performed with all ten eclipses where all orbital parameters were common between 12.8 µm and 15 µm, but the depth and the limb darkening parameters were fitted independently. The resulting eclipse depths are given in Extended Data Table 4.

Data analysis MG. The second data analysis was similar in most respects to the first one, using the Fortran code trafit to analyse individually and globally the light curves. The only difference from the analysis done by ED was that i was not fixed. It was nevertheless under the constraint of the prior used on the transit impact parameter.

Data analysis TJB. For our third data analysis, we continued using the fitting tools in the Eureka! package. For each of our fits, we used a batman eclipse model corrected to account for light travel time as our astrophysical model. Our astrophysical priors were normal priors of $P = 1.5108794 \pm 0.000006$ d (ref. 9), $t_0 = 2459891.015 \pm 0.005$ BJD_TDB (barycentric Julian date, barycentric dynamical time) (ref. 9), which we use to set the time of eclipse, and $F_p/F_\star = 600 \pm 2{,}000$ ppm, and we fixed the following parameters, which are poorly constrained using eclipse-only observations: $i = 89.728°$ (ref. 9), $a/R_\star = 20.843$ (ref. 9) (where a is the semi-major axis on the planet) and $e = 0$ (not important to fit for since e is very small and we are already fitting for the time of eclipse, which would be the main impact of a non-zero eccentricity).

Our systematic noise model consisted of a linear trend in time, a linear decorrelation against the PSF width in each of the x and y directions, and an upward exponential ramp and a downward exponential ramp with weakly constrained amplitudes and timescales (since a single exponential ramp was visually insufficient). We also included a Gaussian process with a Matérn-3/2 kernel (implemented within the celerite package[44]) as a function of time with a uniform prior on the log amplitude and log timescale of $\mathcal{U}(-25, 0)$ and $\mathcal{U}(-7, 0)$ as otherwise our light-curve residuals appeared to show non-negligible red noise. Finally, we also included a white-noise error inflation parameter to account for any inaccuracies in the estimated gain as well as the impact of background noise and any other white-noise components.

Following the same general procedure as ref. 12, we first individually fitted each of the new F1280W observations completely independently of each other (fixing the orbital period to $P = 1.510879$ d (ref. 9) to avoid degeneracies between t_0 and P). Then we performed a fit where we used the same orbital period and time of eclipse for all observations, and then finally we performed a fit where we used the same orbital period, time of eclipse and eclipse depth for all observations. For each of our fits, we used the nested sampling algorithm[45] from the dynesty package[46]. For each fit, we used a number of live points equal to $N_{\mathrm{dim}}(N_{\mathrm{dim}}+1)//2$, where N_{dim} is the number of fitted parameters and // denotes integer division; we also used 'multi' bounds, the 'auto' sampling algorithm and ran the fits until the stopping criterion of $\Delta \log \hat{Z} \leq 0.1$ was met. Ultimately, this required about 70 million log-probability evaluations for each of our three runs to reach convergence, which took up to 78 h. Because this method was so computationally intensive, we were not able perform a further fit with both the F1280W and the F1500W eclipses.

Data analysis POL. The fourth analysis was based on the fact that the time of the eclipse is precisely predicted. Then we just sum the signal in the various integrations occurring during the predicted eclipse duration, narrowed by the uncertainties in the predicted eclipse time (±2 min). We take the sum of the signal in the same number of integrations before the eclipse and after the eclipse. The eclipse is rather far from the beginning of the observation and the drift of the detector is smooth, so we can approximate it by a straight line. Then, from the comparison of the flux before and after the eclipse, we deduce the drop in flux during the eclipse. The difference between this value and the signal during the eclipse measures the depth of the eclipse. To have the value in parts per million, we divide by the star flux. To obtain the star flux we remove the background from the signal. The background represents about 46% of the signal at 15 µm and about 31% at 12.8 µm. The final value is the mean of the five eclipses. The noise is measured in the integration windows before, during and after the eclipse and is compared with the expected photon noise (assuming an electronic gain of 3.5 to go from data number to electrons). We then extrapolate the noise as the square root of the number of integrations in the windows and combine the noise of the five eclipses quadratically to obtain the final eclipse depth noise. We also take into account the uncertainty on the star signal, which is negligible when compared with the photon noise. Note that when combining the five eclipses the noise in the sum of the various eclipses varies as the square root of 5, as expected.

Fiducial joint data analysis. The fiducial joint analysis is the one that led to the results presented in the main text. This analysis uses the light curve from the MG reduction, as these are the ones with the best root mean square of the residual before detrending. Then the joint analysis is very similar to the one of ED and MG. The ten eclipses of TRAPPIST-1 b were fitted with the following jump parameters: $M_\star$, $R_\star$, T_{eff}, [Fe/H], t_0, b, e and TTVs. All priors were adopted from refs. 9,43. The only difference from the ED analysis is in the baseline selection. Baselines include polynomials in time, position and FWHM, with a restriction to not use a degree of >2 to prevent overfitting.

Stellar flux and brightness temperature calculation. We conducted measurements of the star's absolute flux density across all calibrated images, utilizing a 25-pixel aperture (similarly to refs. 12,13). Converting these flux densities from megajanskys per steradian to millijanskys, we calculated mean values of 3.42 ± 0.019 mJy and 2.528 ± 0.022 mJy at 12.8 µm and 15 µm, respectively. To this error of approximately of 0.7% and 0.8%, we added a systematic error of 3%, reflecting the estimated absolute photometric precision of MIRI as indicated in the most recent report on the temporal behaviour of the MIRI reduced count rate. This resulted in combined errors of 0.12 mJy and 0.097 mJy at 12.8 µm and 15 µm, respectively. Our measured flux at 15 µm is therefore within 1σ agreement with the measures of ref. 12 (2.589 ± 0.078 mJy) and ref. 13 (2.559 ± 0.079 mJy). We note that to compute the mean stellar flux value at 12.8 µm we have used only the visits that were acquired in the same conditions: that is to say, visits 2–5. As explained previously in Discussion, for the first 12.8 µm visit TRAPPIST-1 was positioned in the bottom left corner of the full frame and not in the centre as for all the other observations (including the ones from GTO 1177 and GO 2304) (Supplementary Fig. 1). This strategy was supposed to allow for another star in the field for potential comparisons; however, the bottom left region is more impacted by the background and flat-fielding corrections. In that regard, we decided not to include the stellar flux measured from the first visit in calculation of the mean for consistency. We also note that we have reduced all the data with the same version

of the JWST CRDS pipeline (v.7.5.0.3, using the jwst_1089.pmap CRDS context) for all visits (for GTO 1279 and GTO 1177).

Then, by multiplying the measured flux density by the observed occultation depth, we derived a planetary flux density of 1.55 ± 0.29 μJy at 12.8 μm and 2.18 ± 0.25 μJy at 15 μm. We show these results compared with those from ref. 12 in Extended Data Fig. 1. Then, employing Planck's law, we computed the planet's brightness temperature as $T_{\mathrm{bright,\,12.8\,\mu m}} = 424 \pm 28$ K and $T_{\mathrm{bright,\,15\,\mu m}} = 478 \pm 27$ K, to be contrasted with an equilibrium temperature of 508 K computed for a planet with zero albedo and zero heat distribution across its surface.

Potential eclipse depth variability. When we analyse each light curve individually, we observe some indicative variability in the eclipse depth with all data analysis methods at 12.8 μm (Extended Data Table 4) but not at 15 μm (Supplementary Fig. 7). To assess whether this variability is real or not, we performed several statistical tests (Shapiro–Wilk test, Anderson–Darling test and Monte Carlo test). Each statistical test reached the same conclusion, that this variability is currently not significant, and we cannot reject the null hypothesis that all five eclipse depths were drawn from a single normal distribution based on the current observations only. Hence, additional eclipses at 12.8 μm are needed to confirm or reject the depth variability hypothesis. As a thought experiment, if we hypothetically assumed that this time-dependent occultation depth variability at 12.8 μm for TRAPPIST-1 b is real, this would have very interesting implications. Possible explanations include the following.

- The existence of an out-gassing source (volcanoes, geysers and so on) that creates gases or dusts that would absorb the planetary thermal flux at 12.8 μm, but that would then be blown away rapidly by stellar activity (on the timescale of a day, as visits 2 and 3 at 12.8 μm are only one orbital period apart from each other, Supplementary Fig. 7). Interestingly, due to the close proximity to its star and the perpetual excitation of its eccentricity by the other planets, TRAPPIST-1 b is very probably strongly tidally heated[27], which can lead to strong volcanism.
- The existence of photochemical processes between stellar activity and molecules present in a putative atmosphere of TRAPPIST-1 b that results in the creation of molecules or hazes that either absorb or emit strongly at 12.8 μm on the timescale of a day.

Modelling of the thermal emission of the planet

For the stellar spectrum, we used the SPHINX model grid[47] interpolated to TRAPPIST-1's parameters[9,43]. We compared the integrated binned stellar fluxes of this theoretical spectrum weighted by filters F1280W and F1500W and compared them with the measured stellar fluxes (3.42 ± 0.019 mJy and 2.528 ± 0.022 mJy at 12.8 μm and 15 μm, respectively). Similarly to ref. 25, we find that an ~7% correction needs to be applied to the SPHINX synthetic spectrum to match the observations. For the computation of the following emission models (bare surfaces and atmospheres) this corrected SPHINX spectrum was used.

Bare surfaces. The surface emission models used here are the same as the ones presented in ref. 25. These models were generated using the open-source one-dimensional radiative transfer code HELIOS, which computes the temperature–pressure profiles and emission spectra in radiative–convective equilibrium, including the effects of a solid surface[48,49]. Six different surfaces were modelled: basaltic, ultramafic, feldspathic, metal rich, Fe oxidized and granitoid[14,26]. The emission spectrum for each scenario was derived from the wavelength-dependent albedo spectrum of the various surfaces. For the grey albedo emission model, we do not follow the exact methodology of ref. 25, where a constant temperature is assumed across the entire dayside of the planet. Instead, we modelled the theoretical emission spectrum of an airless planet with a Bond albedo A_B in the absence of heat redistribution by considering the planetary flux F_p to be a sum of blackbodies calculated for a grid of $T_{\theta,\phi}$, defined as

$$F_p = \left(\frac{R_p}{d}\right)^2 \left(\int_{-\pi/2}^{\pi/2}\int_{-\pi/2}^{\pi/2} \epsilon_\lambda B_\lambda[T(\theta,\phi)]\cos\theta\cos\phi\,\mathrm{d}\theta\,\mathrm{d}\phi\right), \quad (1)$$

where the emissivity of the planet (ϵ_λ) is constant and equal to $(1 - A_B)$, d is the distance from the observe to the star and B_λ is the spectral radiance of a body for wavelength λ at absolute temperature T, and T depends on the latitude θ and longitude φ on the planet.

For a wavelength-independent albedo, the temperature of the substellar point (at zenith) is independent of that albedo and has a value $T_{\mathrm{dayside,max}} = T_\star\sqrt{\frac{R_\star}{a}}$. The temperature then decreases with increasing latitude and longitude up to the terminator and is fixed to 45 K on the nightside (left panel of Supplementary Fig. 2). From this theoretical definition, we perform a Bayesian analysis, varying the radius of the planet and its albedo, simultaneously fitting the transit spectrum and the eclipse depth. As constraints on the model we use the MIRI eclipse measurements detailed above and the Near Infrared Imager and Slitless Spectrograph (NIRISS)/single object slitless spectroscopy (SOSS) transit transmission spectrum as presented in ref. 50. From this, we derive the value of the Bond albedo that best fits the measurements of the eclipse depths at 12.8 and 15 μm (right panel of Supplementary Fig. 2). The resulting best fit of the NIRISS transmission spectrum is shown in Supplementary Fig. 8.

We derive $A_B = 0.19 \pm 0.08$, which is a higher value than expected for an atmosphereless planet exposed very frequently to important stellar activity, such as TRAPPIST-1 b. Space weathering should markedly lower the albedo of the planet and reduce the spectral contrast via the creation of nanometre-scale iron particles[51]. We note that, considering the error that we derive on the albedo, we do not have evidence against a grey albedo and have mild evidence (1.8σ) against a null-albedo black surface.

Additionally, we compared our measurement with the recently published bare-surface models of ref. 25. For this comparison, we did not fit any parameters and only compared the predictions with the observations and computed the reduced χ^2 of each surface model for two data points and one fitted parameter (Supplementary Table 1). We conclude that the ultramafic surface model is favoured. Alternatively, a highly weathered granitoid surface could be a possibility, but this is out of the scope of this Article as we did not model the effect of space weathering on the bare-surface emission spectra.

Atmospheric models. We constructed 1D and 3D atmospheric models, and compared the measurements. These models are described below.

One-dimensional atmosphere with full heat redistribution. For the atmosphere model of TRAPPIST-1 b, we initially use the set-up from ref. 48 with a pure CO_2 atmosphere and full heat redistribution. We take the surface pressure to be 10 bar and a grey surface albedo of 0.1. The only change with respect to the set-up from ref. 48 is that we mix in hydrocarbon haze particles. This is a rather extreme set-up in terms of heat redistribution efficiency, but we use it as a proof of concept to show the dependence of the atmospheric flux on haze content. For the optical properties of the hydrocarbon haze particles, we use the optEC$_{(s)}$ model as derived in ref. 52 together with Mie theory to convert the refractive index into absorption and scattering cross-sections. In this model, the properties of the hydrocarbon particles are modelled as a function of particle size and band gap, E_g. We fix the size of the particles to be 50 nm, consistent with findings for haze production from CO_2 in the laboratory[53].

We compute the temperature structure of the atmosphere using the radiative transfer code ARCiS[54,55]. Since we consider full heat redistribution in our nominal set-up, we do not use the three-dimensional

(3D) implementation as presented in ref. 55 but an isothermal irradiation with a heat redistribution factor of 0.25. As constraints on the model we use our MIRI eclipse measurements in addition to the NIRISS/SOSS transmission spectrum presented in ref. 50. Our retrieval set-up has only three free parameters: the radius R_p, the haze mass fraction in the atmosphere f_{haze} and the band gap in the hydrocarbon particles E_g. In Supplementary Fig. 3 we present the resulting cornerplot; the resulting best-fit transmission spectrum compared with the NIRISS measurement is shown in Supplementary Fig. 8. As can be seen, the haze mass fraction is well constrained. Interestingly, the band gap is also constrained. This is probably caused by the variation of the albedo as function of E_g. In our simplistic set-up, we consider this result to be preliminary, and more detailed haze models in combination with more constraining observations are required to determine the band gap.

Our median probability model has $f_{haze} = 4.5 \times 10^{-4}$. To show the dependence of the temperature structure in the atmosphere on increasing f_{haze}, we computed models with 0, 10^{-3}, 10^{-1} and 1 times this median value. The results are shown in Fig. 3. We see that for the model with $f_{haze} = 0$ we reproduce the resulting temperature structure as computed by ref. 48, with the exception of the temperatures close to the surface. The differences close to the surface are probably caused by a different treatment of the surface/atmosphere interaction, that is, the lower-boundary condition in the radiative transfer. In our model we force the surface temperature to be the same as the lowest atmospheric grid cell, while ref. 48 allows the temperature to make a jump at the surface. The most striking result is the rapid formation of a strong temperature inversion when a haze is added to the atmosphere. The haze particles are very good absorbers in the optical but absorb much less efficiently in the infrared. In this way they create an inverse greenhouse effect, cooling the lower part of the atmosphere and capturing the stellar radiation higher up. This thermal inversion creates a CO_2 emission feature around 15 μm, which boosts the flux at these wavelengths at the expense of flux at other wavelengths.

We have performed a comparison between ARCiS and ATMO[56,57] to check the robustness of the temperature inversion produced by the heating from hazes in the upper atmosphere. Both models consider a CO_2 atmosphere with a uniform haze layer through the entire atmosphere and a constant albedo of 0.3, and the following parameterization of the haze opacity: κ_1/λ^2 with $\kappa_1 = 0.5\ cm^2\ g^{-1}$ and λ the wavelength in micrometres. The resulting PT profiles and eclipse depth are shown in Supplementary Fig. 4. Both models reproduce a temperature inversion with temperatures of ~500 K at pressures of ~10^{-3} bar and a deep-atmosphere temperature of around ~250 K. The corresponding eclipse depth shows an increase by a factor of ~2 between 12.8 and 15 μm, in agreement with the observations. Differences remain between the two models, probably because of inconsistent parameters (for example, for the stellar irradiation). However, the agreement between the two models is good given the uncertainties of the observations and shows that the inversion is produced robustly without the need to fine tune the models.

3D atmosphere with partial heat redistribution. The two cases presented above, a bare ultramafic rock without any redistribution of heat and a thick atmosphere with full heat redistribution, both provide a decent representation of the data. In this section we explore the intermediate case. A simple equation that can be used to compute the heat redistribution factor for a given atmospheric surface pressure is given in ref. 15. We use this equation to run retrievals where we fix the surface pressure to values of 0.1, 1 and 10 bar but we compute the heat redistribution efficiency using the equations from ref. 15. This allows us to construct a 3D model of the atmosphere including the nightside and thereby make a crude approximation of what a phase-curve observation of the planet might look like. If the hazes are formed by photochemistry on the dayside it is unknown if they will transfer to the nightside. Here we assume they do, so we keep f_{haze} constant. This will cause the thermal inversion to also transport to the nightside. Even though there are many uncertainties in this computation, we consider it a useful exercise to study the potential differences in observed phase curve.

We start our procedure from the median probability model from the previous section. The value for E_g remains fixed while the values for R_p, f_{haze} and the surface albedo are varied to optimize the model with respect to the JWST transit and eclipse data. We construct the 3D atmospheric model using the diffusion concept[55] and we compute the strength of the heat diffusion to the nightside by enforcing the night-to-day ratio computed from the equations from ref. 15.

The equations for heat redistribution depend on the long-wavelength optical depth. Therefore, we iterate on this to find the heat redistribution efficiency. For atmospheres of 0.1, 1 and 10 bar we find heat redistribution factors of 0.62, 0.44 and 0.28 respectively, where lower values mean more efficient heat transport. In ref. 55 the heat redistribution is defined in terms of the integrated flux on the nightside divided by the integrated flux on the dayside. This parameter, the night-to-day ratio, can also be computed following the equations from ref. 15. It has values of 0.05, 0.37 and 0.85 for the 0.1, 1 and 10 bar models respectively. For this definition of the heat redistribution higher values correspond to more efficient transport.

In Supplementary Fig. 5 we show the resulting phase curves of TRAPPIST-1 b in the 15 μm filter for the different atmospheric pressures. We also show the binned simulated MIRI F1500W data that we constructed on the basis of the performances obtained from the reduction of existing 15 μm observations of TRAPPIST-1 taken as part of GTO programme 1177. As can be seen, we should be able to constrain the heat redistribution efficiency, and thereby the surface pressure, by observing the infrared phase curve. Note that if there are no photochemical hazes on the nightside of the planet it is not given that the nightside has a thermal inversion like the dayside. Therefore, it might be that, even with a thick atmosphere, the nightside flux is lower than predicted by our simple model.

Comparison with Solar System bodies. The photochemical haze model presented above is inspired by the hazes in the atmosphere of Titan. Photochemical hazes are predicted to be important in atmospheres of moderately warm exoplanets as well[58]. TRAPPIST-1 b orbits a star very different from the Sun (Extended Data Fig. 2). This makes direct comparison with Solar System planets difficult. In terms of total irradiation, TRAPPIST-1 b lies between Mercury, which receives about twice as much radiation, and Venus, which receives about half that of TRAPPIST-1 b. However, because the central star is so different from the Sun the UV flux received by TRAPPIST-1 b does not have any analogues in the solar system. If we integrate the stellar flux between 100 and 400 nm, using the spatial energy distribution from the Mega-MUSCLES project[32], we find that TRAPPIST-1 b receives about 93% of the UV radiation that Titan receives from the Sun (red patch in Extended Data Fig. 2).

However, if we distinguish the EUV and near-UV contribution of the full UV spectrum, the comparison does not stand anymore. In particular, from an EUV point of view, the TRAPPIST-1 planets receive high EUV irradiations (at least 10^3 times Titan's flux[27]). Such strong EUV can alter the atmospheres though atmospheric escape[59] and can also intensify photochemical reactions in the upper atmosphere, resulting in the formation and accumulation of high-altitude organic haze[27]. In particular, the photodissociation rate of CH_4 (maximized in the 20–150 nm wavelength range) is expected to be higher[60]. We also note that the photodissociation of CO_2 happens in the 120–180 nm spectral region. However, the photolysis of CO_2 creates oxygen radicals that can lead to the destruction of hazes via the oxidization of hydrocarbon photochemical products[61]. The currently most updated UV spectrum of TRAPPIST-1[32] shows a drop of flux between 100 and 300 nm, which could suggest that the photodissociation of CO_2, and therefore the creation of oxygen radicals, is not optimal on TRAPPIST-1 planets, such that the presence of hazes might remain possible even in the presence of CO_2.

Finally, concerning the thermal inversion resulting from the presence of hazes, the feedback of the absorption properties on the atmosphere is discussed in detail in ref. 29. In that paper, a model is presented explaining the thermal inversion observed in, for example, Titan. We note that in our model the thermal inversion does extend to higher pressures because we have a homogeneous mixing efficiency of the hazes throughout the entire atmosphere as opposed to a more realistic layer of haze. When more observations are available more realistic haze models should be explored to investigate the haze properties and hopefully compare them with the hazes found in the atmospheres of Solar System bodies—for example, Titan and Venus.

Data availability

The data used in this Article are associated with JWST GTO programmes 1177 (PI: T.G.) and GTO 1279 (PI: P.-O.L.) and are publicly available from the Mikulski Archive for Space Telescopes (https://mast.stsci.edu) on this link. Additional source data, tables and figures from this work are archived on Zenodo at https://doi.org/10.5281/zenodo.13385020 (ref. 62). Source data are provided with this paper.

Code availability

This work was performed using the following codes to process, extract, reduce and analyse the data: STScI's JWST calibration pipeline[38], Eureka![21], trafit[40], starry[63], exoplanet[64], PyMC3[65], emcee[66], dynesty[46], NumPy[67], Astropy[68] and matplotlib[69].

References

1. Kirkpatrick, J. D., Beichman, C. A. & Skrutskie, M. F. The coolest isolated M dwarf and other 2MASS discoveries. *Astrophys. J.* **476**, 311–318 (1997).
2. Anglada-Escudé, G. et al. A terrestrial planet candidate in a temperate orbit around Proxima Centauri. *Nature* **536**, 437–440 (2016).
3. Zechmeister, M. et al. The CARMENES search for exoplanets around M dwarfs: two temperate Earth-mass planet candidates around Teegarden's Star. *Astron. Astrophys.* **627**, A49 (2019).
4. Gillon, M. et al. Seven temperate terrestrial planets around the nearby ultracool dwarf star TRAPPIST-1. *Nature* **542**, 456–460 (2017).
5. Ment, K. et al. A second terrestrial planet orbiting the nearby M dwarf LHS 1140. *Astron. J.* **157**, 32 (2019).
6. Dreizler, S. et al. RedDots: a temperate 1.5 Earth-mass planet candidate in a compact multiterrestrial planet system around GJ 1061. *Mon. Not. R. Astron. Soc.* **493**, 536–550 (2020).
7. Peterson, M. S. et al. A temperate Earth-sized planet with tidal heating transiting an M6 star. *Nature* **617**, 701–705 (2023).
8. Vanderspek, R. et al. TESS discovery of an ultra-short-period planet around the nearby M dwarf LHS 3844. *Astrophys. J.* **871**, L24 (2019).
9. Agol, E. et al. Refining the transit-timing and photometric analysis of TRAPPIST-1: masses, radii, densities, dynamics, and ephemerides. *Planet. Sci. J.* **2**, 1 (2021).
10. Gillon, M. et al. The TRAPPIST-1 JWST Community Initiative. *Bull. AAS* https://doi.org/10.3847/25c2cfeb.afbf0205 (2020).
11. Morley, C. V., Kreidberg, L., Rustamkulov, Z., Robinson, T. & Fortney, J. J. Observing the atmospheres of known temperate Earth-sized planets with JWST. *Astrophys. J.* **850**, 121 (2017).
12. Greene, T. P. et al. Thermal emission from the Earth-sized exoplanet TRAPPIST-1 b using JWST. *Nature* **618**, 39–42 (2023).
13. Zieba, S. et al. No thick carbon dioxide atmosphere on the rocky exoplanet TRAPPIST-1 c. *Nature* **620**, 746–749 (2023).
14. Mansfield, M. et al. Identifying atmospheres on rocky exoplanets through inferred high albedo. *Astrophys. J.* **886**, 141 (2019).
15. Koll, D. D. B. et al. Identifying candidate atmospheres on rocky M dwarf planets via eclipse photometry. *Astrophys. J.* **886**, 140 (2019).
16. Crossfield, I. J. M. et al. GJ 1252b: a hot terrestrial super-Earth with no atmosphere. *Astrophys. J. Lett.* **937**, L17 (2022).
17. Rackham, B. V., Apai, D. & Giampapa, M. S. The transit light source effect: false spectral features and incorrect densities for M-dwarf transiting planets. *Astrophys. J.* **853**, 122 (2018).
18. Howard, W. S. et al. Characterizing the near-infrared spectra of flares from TRAPPIST-1 during JWST transit spectroscopy. *Astrophys. J.* **959**, 64 (2023).
19. Lim, O. et al. Atmospheric reconnaissance of TRAPPIST-1 b with JWST/NIRISS: evidence for strong stellar contamination in the transmission spectra. *Astrophys. J. Lett.* **955**, L22 (2023).
20. Luger, R., Lustig-Yaeger, J. & Agol, E. Planet–planet occultations in TRAPPIST-1 and other exoplanet systems. *Astrophys. J.* **851**, 94 (2017).
21. Bell, T. J. et al. Eureka!: an end-to-end pipeline for JWST time-series observations. *J. Open Source Softw.* **7**, 4503 (2022).
22. Lyu, X. et al. Super-Earth LHS3844b is tidally locked. *Astrophys. J.* **964**, 152 (2024).
23. Madden, J. & Kaltenegger, L. A catalog of spectra, albedos, and colors of Solar System bodies for exoplanet comparison. *Astrobiology* **18**, 1559–1573 (2018).
24. Takahashi, J., Itoh, Y. & Takahashi, S. Mid-infrared spectroscopy of 11 main-belt asteroids. *Publ. Astron. Soc. Jpn* **63**, 499–511 (2011).
25. Ih, J., Kempton, E. M.-R., Whittaker, E. A. & Lessard, M. Constraining the thickness of TRAPPIST-1 b's atmosphere from its JWST secondary eclipse observation at 15 µm. *Astrophys. J. Lett.* **952**, L4 (2023).
26. Hu, R., Ehlmann, B. L. & Seager, S. Theoretical spectra of terrestrial exoplanet surfaces. *Astrophys. J.* **752**, 7 (2012).
27. Turbet, M. et al. Modeling climate diversity, tidal dynamics and the fate of volatiles on TRAPPIST-1 planets. *Astron. Astrophys.* **612**, A86 (2018).
28. Kislyakova, K. G. et al. Magma oceans and enhanced volcanism on TRAPPIST-1 planets due to induction heating. *Nat. Astron.* **1**, 878–885 (2017).
29. Robinson, T. D. & Catling, D. C. Common 0.1 bar tropopause in thick atmospheres set by pressure-dependent infrared transparency. *Nat. Geosci.* **7**, 12–15 (2014).
30. Bourrier, V. et al. Temporal evolution of the high-energy irradiation and water content of TRAPPIST-1 exoplanets. *Astron. J.* **154**, 121 (2017).
31. Peacock, S., Barman, T., Shkolnik, E. L., Hauschildt, P. H. & Baron, E. Predicting the extreme ultraviolet radiation environment of exoplanets around low-mass stars: the TRAPPIST-1 system. *Astrophys. J.* **871**, 235 (2019).
32. Wilson, D. J. et al. The Mega-MUSCLES spectral energy distribution of TRAPPIST-1. *Astrophys. J.* **911**, 18 (2021).
33. Thompson, M. A., Krissansen-Totton, J., Wogan, N., Telus, M. & Fortney, J. J. The case and context for atmospheric methane as an exoplanet biosignature. *Proc. Natl Acad. Sci. USA* **119**, e2117933119 (2022).
34. Wogan, N., Krissansen-Totton, J. & Catling, D. C. Abundant atmospheric methane from volcanism on terrestrial planets is unlikely and strengthens the case for methane as a biosignature. *Planet. Sci. J.* **1**, 58 (2020).
35. He, C. et al. Sulfur-driven haze formation in warm CO_2-rich exoplanet atmospheres. *Nat. Astron.* **4**, 986–993 (2020).
36. Redfield, S. et al. Report of the Working Group on Strategic Exoplanet Initiatives with HST and JWST. Preprint at http://arxiv.org/abs/2404.02932 (2024).
37. Stetson, P. B. DAOPHOT: a computer program for crowded-field stellar photometry. *Publ. Astron. Soc. Pac.* **99**, 191–222 (1987).
38. Bushouse, H. et al. JWST calibration pipeline. *Zenodo* https://doi.org/10.5281/zenodo.7577320 (2023).

39. CRDS: Calibration Reference Data System for HST and JWST. *GitHub* https://github.com/spacetelescope/crds (2022).
40. Gillon, M. et al. Improved precision on the radius of the nearby super-Earth 55 Cnc e. *Astron. Astrophys.* **539**, A28 (2012).
41. Gillon, M. et al. Search for a habitable terrestrial planet transiting the nearby red dwarf GJ 1214. *Astron. Astrophys.* **563**, A21 (2014).
42. Mandel, K. & Agol, E. Analytic light curves for planetary transit searches. *Astrophys. J.* **580**, L171–L175 (2002).
43. Ducrot, E. et al. TRAPPIST-1: global results of the *Spitzer* Exploration Science Program Red Worlds. *Astron. Astrophys.* **640**, A112 (2020).
44. Foreman-Mackey, D., Agol, E., Ambikasaran, S. & Angus, R. Fast and scalable Gaussian process modeling with applications to astronomical time series. *Astron. J.* **154**, 220 (2017).
45. Skilling, J. Nested sampling for general Bayesian computation. *Bayesian Anal.* **1**, 833–859 (2006).
46. Speagle, J. S. dynesty: a dynamic nested sampling package for estimating Bayesian posteriors and evidences. *Mon. Not. R. Astron. Soc.* **493**, 3132–3158 (2020).
47. Iyer, A. R., Line, M. R., Muirhead, P. S., Fortney, J. J. & Gharib-Nezhad, E. The SPHINX M-dwarf spectral grid. I. Benchmarking new model atmospheres to derive fundamental M-dwarf properties. *Astrophys. J.* **944**, 41 (2023).
48. Malik, M. et al. Analyzing atmospheric temperature profiles and spectra of M dwarf rocky planets. *Astrophys. J.* **886**, 142 (2019).
49. Whittaker, E. A. et al. The detectability of rocky planet surface and atmosphere composition with JWST: the case of LHS 3844b. *Astron. J.* **164**, 258 (2022).
50. Lim, O. et al. JWST reconnaissance transmission spectroscopy of the Earth-sized exoplanet TRAPPIST-1 b. *Bull. AAS* **55**, 2023n2i125p06 (2023).
51. Domingue, D. L. et al. Mercury's weather-beaten surface: understanding Mercury in the context of lunar and asteroidal space weathering studies. *Space Sci. Rev.* **181**, 121–214 (2014).
52. Jones, A., Noll, S., Kausch, W., Szyszka, C. & Kimeswenger, S. An advanced scattered moonlight model for Cerro Paranal. *Astron. Astrophys.* **560**, A91 (2013).
53. He, C. et al. Laboratory simulations of haze formation in the atmospheres of super-Earths and mini-Neptunes: particle color and size distribution. *Astrophys. J. Lett.* **856**, L3 (2018).
54. Min, M., Ormel, C. W., Chubb, K., Helling, C. & Kawashima, Y. The ARCiS framework for exoplanet atmospheres: modelling philosophy and retrieval. *Astron. Astrophys.* **642**, A28 (2020).
55. Chubb, K. L. & Min, M. Exoplanet atmosphere retrievals in 3D using phase curve data with ARCiS: application to WASP-43b. *Astron. Astrophys.* **665**, A2 (2022).
56. Tremblin, P. et al. Fingering convection and cloudless models for cool brown dwarf atmospheres. *Astrophys. J.* **804**, L17 (2015).
57. Drummond, B. et al. The effects of consistent chemical kinetics calculations on the pressure–temperature profiles and emission spectra of hot Jupiters. *Astron. Astrophys.* **594**, A69 (2016).
58. Kawashima, Y. & Ikoma, M. Theoretical transmission spectra of exoplanet atmospheres with hydrocarbon haze: effect of creation, growth, and settling of haze particles. I. Model description and first results. *Astrophys. J.* **853**, 7 (2018).
59. Luger, R. & Barnes, R. Extreme water loss and abiotic O_2 buildup on planets throughout the habitable zones of M dwarfs. *Astrobiology* **15**, 119–143 (2015).
60. Hu, R., Peterson, L. & Wolf, E. T. O_2- and CO-rich atmospheres for potentially habitable environments on TRAPPIST-1 planets. *Astrophys. J.* **888**, 122 (2020).
61. Arney, G. N. et al. Pale orange dots: the impact of organic haze on the habitability and detectability of Earthlike exoplanets. *Astrophys. J.* **836**, 49 (2017).
62. Ducrot, E. Products of "Combined analysis of the 12.8 and 15 μm JWST/MIRI eclipse observations of TRAPPIST-1 b" [Data set]. *Zenodo* https://doi.org/10.5281/zenodo.13385020 (2024).
63. Luger, R. et al. starry: analytic occultation light curves. *Astron. J.* **157**, 64 (2019).
64. Foreman-Mackey, D. et al. exoplanet: gradient-based probabilistic inference for exoplanet data & other astronomical time series. *J. Open Source Softw.* **6**, 3285 (2021).
65. Salvatier, J., Wiecki, T. V. & Fonnesbeck, C. Probabilistic programming in Python using PyMC3. *PeerJ Comput. Sci.* **2**, e55 (2016).
66. Foreman-Mackey, D., Hogg, D. W., Lang, D. & Goodman, J. emcee: the MCMC hammer. *PASP* **125**, 306 (2013).
67. Harris, C. R. et al. Array programming with NumPy. *Nature* **585**, 357–362 (2020).
68. Robitaille, T. P. et al. Astropy: a community Python package for astronomy. *Astron. Astrophys.* **558**, A33 (2013).
69. Hunter, J. D. Matplotlib: a 2D graphics environment. *Comput. Sci. Eng* **9**, 90–95 (2007).

Acknowledgements

We thank M. Turbet and F. Selsis for discussion regarding the modelling of a putative atmosphere of TRAPPIST-1 b and its likelihood. We thank B. Charnay for discussion regarding photochemical haze formation processes and comparison with Titan. We thank J. Ih for sharing their bare-surface models published in ref. 25 and for useful discussion regarding the calculation of the Bond albedo. We thank O. Lim for sharing their transmission spectra of TRAPPIST-1 b obtained from the reduction and analysis of JWST/NIRISS data and published in their paper ref. 19. We thank E. Agol for his help on planetary flux estimation equations. Finally, we thank A. Iyer for providing the SPHINX stellar spectrum model extrapolated on TRAPPIST-1's parameters. This work is based on observations made with the NASA/ESA/CSA JWST. The data were obtained from the Mikulski Archive for Space Telescopes at the Space Telescope Science Institute, which is operated by the Association of Universities for Research in Astronomy, Inc., under NASA contract NAS 5-03127 for JWST. These observations are associated with programme 1279. MIRI draws on the scientific and technical expertise of the following organizations: NASA Ames Research Center, USA; Airbus Defence and Space, UK; CEA-Irfu, Saclay, France; Centre Spatial de Liège, Belgium; Consejo Superior de Investigaciones Científicas, Spain; Carl Zeiss Optronics, Germany; Chalmers University of Technology, Sweden; Danish Space Research Institute, Denmark; Dublin Institute for Advanced Studies, Ireland; European Space Agency, The Netherlands; ETCA, Belgium; ETH Zurich, Switzerland; Goddard Space Flight Center, USA; Institut d'Astrophysique Spatiale, France; Instituto Nacional de Técnica Aeroespacial, Spain; Institute for Astronomy, Edinburgh, UK; Jet Propulsion Laboratory, USA; Laboratoire d'Astrophysique de Marseille (LAM), France; Leiden University, The Netherlands; NOVA Opt-IR group at Dwingeloo, The Netherlands; Northrop Grumman, USA; Max-Planck-Institut für Astronomie (MPIA), Heidelberg, Germany; Laboratoire d'Etudes Spatiales et d'Instrumentation en Astrophysique (LESIA), France; Paul Scherrer Institut, Switzerland; Raytheon Vision Systems, USA; RUAG Aerospace, Switzerland; Rutherford Appleton Laboratory (RAL Space), UK; Space Telescope Science Institute, USA; Toegepast Natuurwetenschappelijk Onderzoek (TNO-TPD), The Netherlands; UK Astronomy Technology Centre, UK; University College London, UK; University of Amsterdam, The Netherlands; University of Arizona, USA; University of Bern, Switzerland; University of Cardiff, UK; University of Cologne, Germany; University of Ghent, Belgium; University of Groningen, The Netherlands; University of Leicester, UK; University of Leuven, Belgium; University of Stockholm, Sweden. The following national and international funding agencies funded and supported the MIRI development: NASA; European Space Agency (ESA); Belgian

Science Policy Office (BELSPO); Centre Nationale d'Etudes Spatiales (CNES); Danish National Space Centre; Deutsches Zentrum für Luft- und Raumfahrt (DLR); Enterprise Ireland; Ministerio De Economalia y Competividad; Netherlands Research School for Astronomy (NOVA); Netherlands Organisation for Scientific Research (NWO); Science and Technology Facilities Council; Swiss Space Office; Swedish National Space Agency; UK Space Agency. E.D. acknowledges support from the innovation and research Horizon 2020 programme in the context of the Marie Sklodowska-Curie subvention 945298 as well as from the Paris Observatory–PSL fellowship. M. Gillon is FRS-FNRS Research Director. His contribution to this work was done in the framework of the PORTAL project funded by the Federal Public Planning Service Science Policy (BELSPO) within its BRAIN-be: Belgian Research Action through the Interdisciplinary Networks programme. P.-O.L., C.C., A.D., R.G. and A.C. acknowledge funding support from CNES. T.G. and T.J.B. acknowledge support from NASA in WBS 411672.07.04.01.02. O.A., I.A., B.V. and P.R. thank the ESA and BELSPO for their support in the framework of the PRODEX Programme. D.B. is supported by Spanish MCIN/AEI/10.13039/501100011033 grants PID2019-107061GB-C61 and MDM-2017-0737. L.D. acknowledges funding from the KU Leuven Interdisciplinary Grant (IDN/19/028), the European Union H2020-MSCA-ITN-2019 under grant 860470 (CHAMELEON) and the FWO research grant G086217N. J.P. acknowledges financial support from the UK Science and Technology Facilities Council and the UK Space Agency. G. Ostlin acknowledges support from the Swedish National Space Board and the Knut and Alice Wallenberg Foundation. P.T. acknowledges support by the European Research Council under grant agreement ATMO 757858. E.D. has received funding from the European Union's Horizon 2020 research and innovation programme under the Marie Skłodowska-Curie actions grant agreement 945298-ParisRegionFP as well as from the Paris Observatory–PSL fellowship. L.C. acknowledges support by grant PIB2021-127718NB-100 from the Spanish Ministry of Science and Innovation/State Agency of Research MCIN/AEI/10.13039/501100011033. E.F.v.D. acknowledges support from A-ERC grant 101019751 MOLDISK. T.P.R. acknowledges support from the ERC 743029 EASY. G. Olofsson acknowledges support from SNSA. P.P. thanks the Swiss National Science Foundation (SNSF) for financial support under grant number 200020_200399. O.A. is a senior research associate of the Fonds de la Recherche Scientifique—FNRS.

Author contributions

All authors played an important role in one or more of the following: development of the original proposal, management of the project, definition of the target list and observation plan, analysis of the data, theoretical modelling and preparation of this Article. Some specific contributions are listed as follows. P.-O.L. is PI of the JWST MIRI GTO European consortium programme dedicated to JWST observations of exoplanet atmospheres; R.W. is co-lead of the programme. E.D. provided overall programme leadership and management of the TRAPPIST-1 b working group. P.-O.L., T.G., J.B. and T.H. designed the observational programme and set the observing parameters. A.D. generated simulated data for prelaunch testing of the data reduction methods. E.D., M. Gillon, T.J.B. and P.-O.L. reduced the data, modelled the light curves and produced the eclipse depth. M.M. and P.T. generated theoretical models to interpret the data. E.D. led the writing of the Article, and M. Gillon, T.J.B., P.-O.L., T.G. and M.M. made notable contributions to the writing. G.W. is the European PI of the JWST MIRI instrument, P.-O.L., T.H., M. Güdel, B.V., L.C., E.F.v.D., T.P.R. and G. Olofsson are European co-PIs and O.A., A.M.G., L.D., R.W., O.K., J.P., G. Ostlin, D.R. and D.B. are European co-Investigators. T.G. is a US co-Investigator of the JWST MIRI instrument. A.G. led the MIRI instrument testing and commissioning effort.

Competing interests

The authors declare no competing interests.

Additional information

Extended data is available for this paper at https://doi.org/10.1038/s41550-024-02428-z.

Supplementary information The online version contains supplementary material available at https://doi.org/10.1038/s41550-024-02428-z.

Correspondence and requests for materials should be addressed to Elsa Ducrot.

Peer review information *Nature Astronomy* thanks Nicolas Cowan, Nestor Espinoza and the other, anonymous, reviewer(s) for their contribution to the peer review of this work.

Reprints and permissions information is available at www.nature.com/reprints.

Publisher's note Springer Nature remains neutral with regard to jurisdictional claims in published maps and institutional affiliations.

Elsa Ducrot[1,2,27] ✉, Pierre-Olivier Lagage[2,27], Michiel Min[3], Michaël Gillon[4], Taylor J. Bell[5,6], Pascal Tremblin[7], Thomas Greene[6], Achrène Dyrek[2], Jeroen Bouwman[8], Rens Waters[3,9,10], Manuel Güdel[11,12], Thomas Henning[8], Bart Vandenbussche[13], Olivier Absil[14], David Barrado[15], Anthony Boccaletti[1], Alain Coulais[2,16], Leen Decin[13], Billy Edwards[3], René Gastaud[2,17], Alistair Glasse[18], Sarah Kendrew[19], Goran Olofsson[20], Polychronis Patapis[12], John Pye[21], Daniel Rouan[1], Niall Whiteford[22], Ioannis Argyriou[13], Christophe Cossou[17], Adrian M. Glauser[12], Oliver Krause[8], Fred Lahuis[23], Pierre Royer[13], Silvia Scheithauer[8], Luis Colina[15], Ewine F. van Dishoeck[24], Göran Ostlin[25], Tom P. Ray[26] & Gillian Wright[18]

[1]LESIA, Observatoire de Paris, CNRS, Université Paris Diderot, Université Pierre et Marie Curie, Meudon, France. [2]Université Paris-Saclay, Université Paris Cité, CEA, CNRS, AIM, Gif-sur-Yvette, France. [3]SRON Netherlands Institute for Space Research, Leiden, The Netherlands. [4]Astrobiology Research Unit, University of Liège, Liège, Belgium. [5]Bay Area Environmental Research Institute, NASA's Ames Research Center, Moffett Field, CA, USA. [6]Space Science and Astrobiology Division, NASA's Ames Research Center, Moffett Field, CA, USA. [7]Maison de la Simulation, Université Paris-Saclay, UVSQ, CNRS, CEA, Gif-sur-Yvette, France. [8]Max-Planck-Institut für Astronomie (MPIA), Heidelberg, Germany. [9]Department of Astrophysics/IMAPP, Radboud University,

Nijmegen, The Netherlands. [10]HFML–FELIX, Radboud University, Nijmegen, The Netherlands. [11]Department of Astrophysics, University of Vienna, Vienna, Austria. [12]Institute for Particle Physics and Astrophysics, ETH Zürich, Zurich, Switzerland. [13]Institute of Astronomy, KU Leuven, Leuven, Belgium. [14]STAR Institute, Université de Liège, Liège, Belgium. [15]Centro de Astrobiología (CAB), CSIC-INTA, Villanueva de la Cañada, Spain. [16]LERMA, Observatoire de Paris, Université PSL, Sorbonne Université, CNRS, Paris, France. [17]Université Paris-Saclay, CEA, IRFU, Gif-sur-Yvette, France. [18]UK Astronomy Technology Centre, Royal Observatory, Edinburgh, UK. [19]European Space Agency, Space Telescope Science Institute, Baltimore, MD, USA. [20]Department of Astronomy, AlbaNova University Center, Stockholm University, Stockholm, Sweden. [21]Space Park Leicester, School of Physics & Astronomy, University of Leicester, Leicester, UK. [22]Department of Astrophysics, American Museum of Natural History, New York, NY, USA. [23]SRON Netherlands Institute for Space Research, Groningen, The Netherlands. [24]Leiden Observatory, Leiden University, Leiden, The Netherlands. [25]Oskar Klein Centre, Department of Astronomy, Stockholm University, Stockholm, Sweden. [26]School of Cosmic Physics, Dublin Institute for Advanced Studies, Dublin, Ireland. [27]These authors contributed equally: Elsa Ducrot, Pierre-Olivier Lagage. ✉e-mail: elsa.ducrot@cea.fr

https://doi.org/10.1038/s41550-024-02428-z

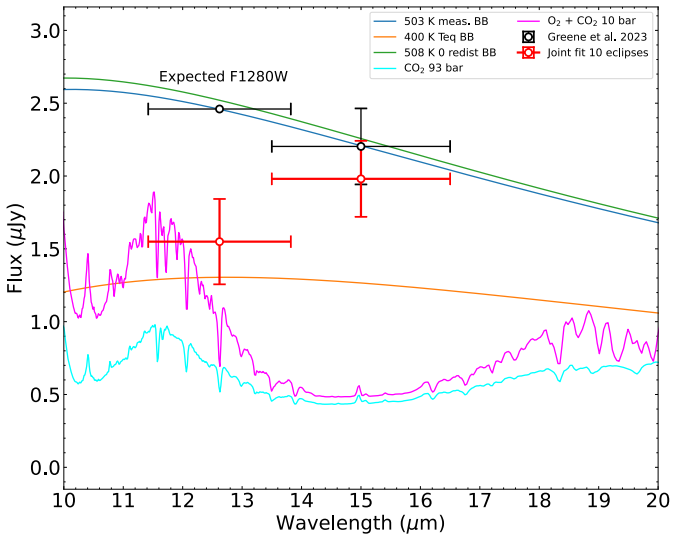

Extended Data Fig. 1 | Planetary flux of TRAPPIST-1 b versus wavelength, from measurements and models. The black dot with its error bar is the measured flux by ref. 12 from the analysis of 5 visits at 15μm, the black dot without an error bar is the expected flux in the F1280W filter for T_B = 503 K. The planetary flux computed from this work is shown with red dots at 12.8 μm and 15 μm. Fluxes are derived from our "fiducial" joint analysis and the error bar in flux show their 1σ uncertainties. The error bar in wavelength stands for the width of the filter in each band. The blue curve shows the blackbody curve expected for a dayside temperature of 503 K, the green curve shows the blackbody curve expected for 508 K apparent dayside temperature predicted for zero heat redistribution and no internal heating, and the orange curve shows the blackbody curve expected for T_{eq} = 400 K temperature for isotropic redistribution of stellar heating.

https://doi.org/10.1038/s41550-024-02428-z

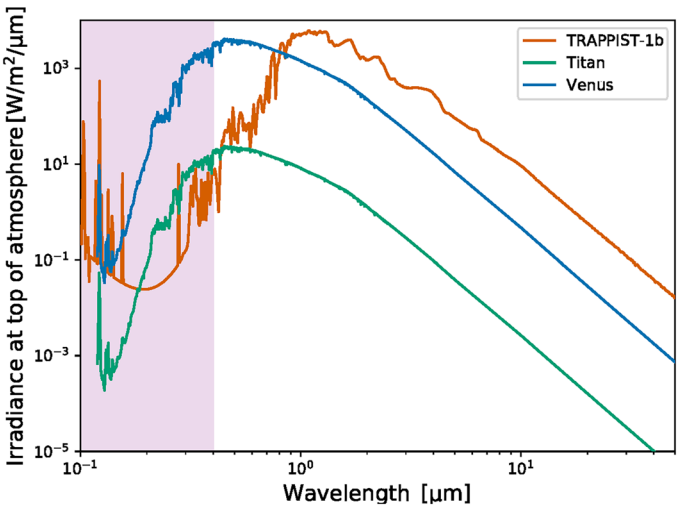

Extended Data Fig. 2 | Comparison of the irradiance at the top of the atmosphere for TRAPPIST-1b, Titan and Venus. For the spectra of Titan and Venus we used the scaled standard Solar irradiance spectrum at air mass zero (AM0). For TRAPPIST-1b the spectrum from the Mega-MUSCLES project is used[32]. The UV part of the spectrum is indicated by the violet band.

https://doi.org/10.1038/s41550-024-02428-z

Extended Data Table 1 | Summary of the observations in JWST program GTO 1279

	visit 1	visit 2	visit 3	visit 4	visit 5
date	21 Nov. 2022	06 July. 2023	07 July. 2023	15 July. 2023	23 July. 2023
start time	17:52:02	09:18:31	21:34:45	11:08:44	00:09:00
end time	21:45:05	13:11:34	01:27:49	15:01:48	04:02:03
duration (h)	3.21	3.88	3.88	3.88	3.88
N_{int}	280	315	315	315	315
N_{groups}/int	17	15	15	15	15

N_{int} = number of integrations during the sequence. N_{groups} = number of groups of observations per integration.

https://doi.org/10.1038/s41550-024-02428-z

Extended Data Table 2 | Details of the different data reduction methods

Stage	Step	ED reduction	MG reduction	TB reduction	POL reduction
Stage 1	-STScI stage 1 run?	yes	yes	yes	No
	-Ramp weighting	default	uniform	default	No ramp fitting
Stage 2	- Skip Photom?	yes	yes	yes	yes
Stage 3	- How to get centroid parameters?	2D Gaussian fit to target	2D Gaussian fit to target	2D Gaussian fit to target	2D Gaussian fit to target
	-Aperture shape	circle	circle	cirle	circle
	-Aperture radius	5 pixels radius around the centroid at 12.8μm and 15μm	[3.5, 3.5, 3.5, 3.5, 3.5] pixels at 12.8μm and [3.5, 3.8, 3.8, 3.8, 3.8] at 15μm pixels around the center	5 pixels radius at 12.8μm and 8 pixels radius at 15μm	4 pixels radius
	-Background aperture size	12-30 pixels for each visit	30 - 45 pixels for each visit	14–34 pixels	30-45 pixels
	-Background subtraction method	subtracted the median calculated within the annulus from the whole frame	subtracted the median calculated within the annulus from the whole frame, after discarding 3σ outliers	Subtracted the median within the annulus after first removing 5σ outliers along the time axis	No background subtraction
	-Outlier rejection/time series clipping	sigma clipping set to 4, no exposure removed	20min-4σ median filtering, 3.5% of exposures removed on average	Removed 3σ outliers with respect to a 10-integration wide boxcar filter	outliers at 5 sigmas, 6 to 9 percents of integration discarded

The details of the four pipelines (last four columns) are described in the Data Reduction section of the Methods

https://doi.org/10.1038/s41550-024-02428-z

Extended Data Table 3 | Details of the different data analysis methods

Step	ED analyses	MG analyses	TB analyses
-Sampling method	MH-MCMC	MH-MCMC	Nested Sampling using `dynesty`[47]
-Setting	2 chains of 100000 steps	2 chains of 100000 steps	$N_{\rm dim}(N_{\rm dim}+1)//2$ live points, bounds='multi', sample='auto', $\Delta \log \hat{\mathcal{Z}} \leq 0.1$
-1 chain to find correction factors	yes	yes	no
-Free planetary parameters	$(R_p/R_\star)^2$, $F_p/F_\star$, b, e, t_0 (for individual fits), TTVs (for join fits)	$(R_p/R_\star)^2$, $F_p/F_\star$, b, e, TTVs	$F_p/F_\star$, t_0, P (for joint fits)
-Free stellar parameters	$R_\star$, $M_\star$, T_{eff}, [Fe/H]	$R_\star$, $M_\star$, T_{eff}, [Fe/H]	None
-Potential polynomial on systematics	ramp, x, y, $FWHM_x$, $FWHM_y$	ramp, x, y, $FWHM_x$, $FWHM_y$	ramp, $FWHM_x$, $FWHM_y$, GP
-RMS of the residuals at 12.8μm (ppm)	[711, 827, 728, 733, 882]	[672, 784, 739, 724, 758]	[975, 883, 788, 912, 921]
-RMS of the residuals at 15μm (ppm)	[1015, 892, 1028, 1250, 1041]	[965, 824, 859, 989, 899]	[1284, 1145, 1038, 1406, 1041]

This Table concerns specifically the fitting of the transit curve.

https://doi.org/10.1038/s41550-024-02428-z

Extended Data Table 4 | Derived eclipse depth with various approaches and fitting method

Fit	ED results	MG results	TB results	POL results
Individual fit for each 5 visits at 12.8μm	[430 ± 163, 465 ± 140, 760±149, 396± 145, 333 ± 150]	[433 ± 173, 482 ± 198, 793±139, 305± 134, 332 ± 169]	[460 ± 340, 600 ± 180, 690±220, 530± 150, 310 ± 220]	[426 ± 129, 539 ± 145, 640±152, 365± 158, 211 ± 155]
Individual fit for each 5 visits at 15μm	[994 ± 187, 691 ± 169, 798±282, 821± 229, 736 ± 259]	[771 ± 176, 632 ± 252, 822±207, 815± 200, 524 ± 189]	[790 ± 210, 510 ± 210, 950±170, 820± 220, 829 ± 200]	[806 ± 177, 585 ± 174, 780±181, 758± 176, 776 ± 164]
Joint fit of the 5 visits at 12.8μm	463 ± 87	413 ± 82	534 ± 81	436 ± 70
Joint fit of the 5 visits at 15μm	823 ± 87	718 ± 91	899 ± 99	741 ± 80
Global joint fit of all 10 visits, 12.8μm	431 ± 90	401 ± 78	N/A	NA
Global joint fit of all 10 visits, 15μm	839 ± 109	718 ± 88	N/A	NA
"fiducial" global joint fit at 12.8μm	452 ± 86			
"fiducial" global joint fit at 15μm	775 ± 90			

This Table provides all results from the various approaches and fits (individual, joint per band, joint with all eclipses).